Supporting Information: Identification of Water Hexamer on Cu(111) Surfaces

Sai Duan,[†,¶] Igor Ying Zhang,[†,¶] Zhen Xie,[‡] and Xin Xu[*,†]

†*Collaborative Innovation Center of Chemistry for Energy Materials, Shanghai, Key Laboratory of Molecular Catalysis and Innovative Materials, MOE Key Laboratory of Computational Physical Sciences, Department of Chemistry, Fudan University, Shanghai 200433, People's Republic of China*

‡*Department of Theoretical Chemistry and Biology, School of Engineering Sciences in Chemistry, Biotechnology and Health, KTH Royal Institute of Technology, S-106 91 Stockholm, Sweden*

¶*Contributed equally to this work*

E-mail: xxchem@fudan.edu.cn

1 Computational Details

In the present calculations, all geometric and electronic structures were calculated with the optB86b-DF[S1] functional as implemented in the Vienna *ab initio* simulation package (VASP).[S2] The single-point calculations of vdW-DF2[S3] and SCAN[S4] were then carried out at the optimized geometries of optB86b-DF. The calculated lattice constant of Cu was 3.627 Å which is in good agreement with the experimental value[S5] of 3.6146 Å as well as previous theoretical result[S6] of 3.623 Å. Three layers of $(4\sqrt{3} \times 8)$ supercells of the Cu(111) slab

with periodic boundary conditions were used for the Cu substrate. In the practical calculations, plane-wave basis sets with energy cutoff of 500 eV and the projector augmented-wave pseudopotentials[S7,S8] were used for valence and core electrons, respectively. Enough vacuum layer (larger than 20 Å) was added along the z axis in the supercell, and the dipole correction[S9,S10] was used to avoid the artificial interactions. To obtain the accurate force, the wavefunction criteria was set to 1.0×10^{-8} eV and the projection operators are evaluated in reciprocal space.

For the optimization, frequency, and molecular dynamic calculations, a $2\times2\times1$ mesh of the Monkhorst-Pack grid[S11] was used for the k-point sampling, which generated 4 k points in the irreducible Brillouin zone for the Brillouin zone integration. The Methfessel and Paxton method[S12] was adopted for improving convergence of the electronic structure calculations, and the total energies were extrapolated to 0 K. During the geometrical optimization, the two bottom slab layers were fixed to mimic the Cu bulk, while all other atoms were allowed to relax in all directions. The force criterion was set to 0.01 eV/Å. Based on the optimized geometries, the central finite difference with displacement of 0.01 Å was used for frequency calculations with all atoms of the substrate fixed. Based on the calculated frequency, the quasi-RRHO approach[S13] proposed by Grimme was used to calculated the Gibbs free energy. For ab initio molecular dynamics simulations, the relaxation of all degrees of the freedom of the topmost Cu(111) layer and the adsorbates was allowed. The Nosé algorithm was used to construct the required canonical ensemble with temperature of 10 K. The time step was set to 1.0 fs and the Nosé-mass was set to corresponding to period of 40 time steps. The total time evolution of the molecular dynamic simulations was 300 fs. It is noted that even with the inclusion of the van der Waals interaction, DFT-based simulations predicted melting points of water were $360-325$ K[S14] that are $32\%-19\%$ larger than the correct one of 273.15 K. Thus, to exclude the effects of the temperature difference between the simulations and the real situations, we performed another AIMD simulation under the temperature of 13 K, which is the upper limit of 30% higher than that used in the experiments (Figure S5).

In the present work, adsorption energy is calculated as

$$E_{\mathrm{ads}} = 6E_{\mathrm{H_2O}} + E_{\mathrm{Cu(111)}} - E_{\mathrm{(H_2O)_6/Cu(111)}} \tag{S1}$$

where $E_{\mathrm{H_2O}}$, $E_{\mathrm{Cu(111)}}$, and $E_{\mathrm{(H_2O)_6/Cu(111)}}$ are energies of the isolated water monomer, the clean Cu(111) surface, and the adsorption complex, respectively. We note that E_{ads} could be further decomposed as

$$E_{\mathrm{ads}} = \Delta E_{\mathrm{int}} + \Delta E^{\mathrm{def}}_{\mathrm{Cu(111)}} + \Delta E^{\mathrm{coh}}_{\mathrm{(H_2O)_6}}$$

where $\Delta E_{\mathrm{int}} = E^{i}_{\mathrm{Cu(111)}} + E^{i}_{\mathrm{(H_2O)_6}} - E_{\mathrm{(H_2O)_6/Cu(111)}}$ is the interaction energy between water hexamer and Cu(111), $\Delta E^{\mathrm{def}}_{\mathrm{Cu(111)}} = E_{\mathrm{Cu(111)}} - E^{i}_{\mathrm{Cu(111)}}$ is the deformation energy of the substrate, and $\Delta E^{\mathrm{coh}}_{\mathrm{(H_2O)_6}} = 6E_{\mathrm{H_2O}} - E^{i}_{\mathrm{(H_2O)_6}}$ is the cohesive energy of water hexamer. Here the superscript "i" represents the extracted in-situ geometry from the adsorption complex. Because of a negligible charge transfer between water hexamer and the inert substrate (Table S1), it is most important to calibrate the energy of water cluster in order to have an improved description of E_{ads}. Hence, we have

$$E_{\mathrm{ads}}(\mathrm{H}) = E_{\mathrm{ads}} + \left(\Delta E^{\mathrm{coh}}_{\mathrm{(H_2O)_6}}(\mathrm{H}) - \Delta E^{\mathrm{coh}}_{\mathrm{(H_2O)_6}}\right) \tag{S2}$$

where $\Delta E^{\mathrm{coh}}_{\mathrm{(H_2O)_6}}(\mathrm{H})$ is the cohesive energy at a high level theory.

For high-level calibrations, the hybrid B3LYP-D3(BJ) calculations were preformed in conjunction with a very large Gaussian-type basis set of aug-cc-pV5Z using the Gaussian suite of programme.[S15] The Q-Chem package was used to perform the calculations of ωB97X-2.[S16] We extrapolated the frozen-core ωB97X-2 results to the complete basis-set limit from aug-cc-pVTZ and QZ, which was recommanded by the developers.[S16] The calculations of the doubly hybrid approximations of XYG3 and XYGJ-OS, as well as those of CCSD(T), were forzen-core and performed using the FHI-aims package in the numerical atom-centered

orbital (NAO) framework.[S17,S18] The NAO basis set used for XYG3 and XYGJ-OS was NAO-VCC-5Z,[S19] while the CCSD(T) results were extrapolated to the complete basis-set limit from NAO-VCC-4Z and 5Z.

Constant current scanning tunneling microscope (STM) images were calculated by the Tersoff-Hamann approximation[S20] that properly weights all the contributions from k-points inside the bias window, i.e.,

$$I \propto \int_{-\infty}^{+\infty} \left[f\left(\epsilon\right) - f\left(\epsilon + eV\right) \right] \rho_{\mathrm{T}}\left(\epsilon + eV\right) \rho_{\mathrm{S}}\left(\mathbf{r}_0, \epsilon\right) d\epsilon \tag{S3}$$

where f is the Fermi-Dirac distribution function, ϵ is the energy level, V is the applied bias voltage, and

$$\begin{aligned} \rho_{\mathrm{T}} &\propto e^{-2\sqrt{2\kappa_\mu} R} \\ \rho_{\mathrm{S}} &= \sum_v \left| \Psi_v(\mathbf{r}_0) \right|^2 \delta\left(E_v - \epsilon\right). \end{aligned} \tag{S4}$$

Here κ_μ and R are the workfunction and curvature of the tip, respectively, Ψ_v and E_v are the eigenfunction and eigenvalue of the effective one-electron orbital of the sample, respectively. It should be noted that the Tersoff-Hamann approximation works perfectly when the tip is more than $5-6$ Å above the sample.[S21] As a rule of thumb, the tunneling resistance should be larger than $10-100$ MΩ.[S21] This perquisite is fully fulfilled because the tunneling resistance is around 1.8×10^3 MΩ as determined in the experiments (20 mV, 11 pA).[S22] In piratical calculations, to obtain the accurate electronic structure of the substrate and sufficiently sample the relatively narrow bias window (20 mV) used in experiments, a $12 \times 12 \times 1$ mesh of the Monkhorst-Pack grid[S11] that generated 74 k-points in the irreducible Brillouin zone and the tetrahedron method with Blöchl corrections[S7] were used. For tips with low workfunction (Figure 1b in the main text), the isovalue of 7.0×10^{-6} e/Å^3 was adopted, meanwhile, for high workfunction tips (Figure 1c in the main text), 2.5×10^{-5} e/Å^3 was used to maintenance the same tunneling current. All calculated images were filtered by the

Gaussian smoothing with bandwidth of 1 Å. In addition, an area with radius of 3.0 Å was averagely integrated to mimic the low spatial resolution. The charge densities for Bader charge analysis[S23,S24] were calculated at the same level of the STM simulations.

2 The experimental STM images

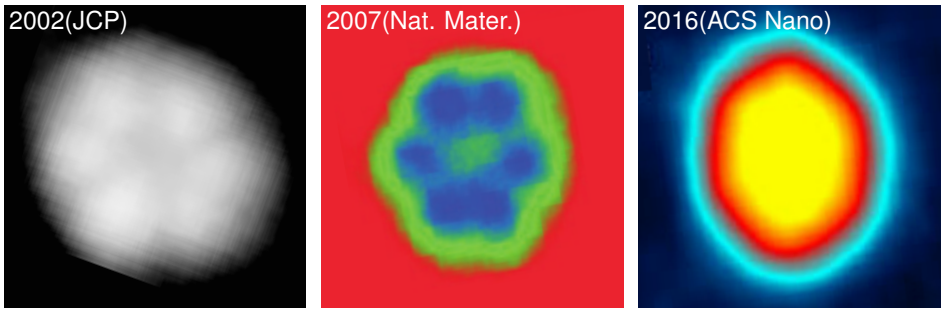

Figure S1: Experimentally reported STM images of water hexamer adsorbed on Cu(111) surface. Adapted from Ref. S25, S26, and S27, and (from left to right).

3 Some other configurations of adsorbed water hexamer

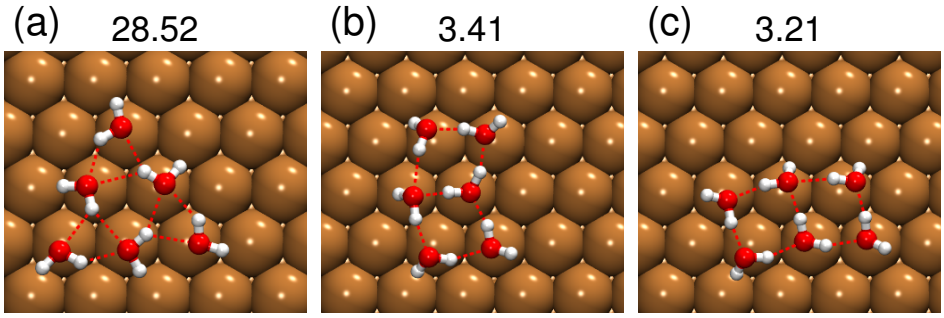

Figure S2: Optimized structures of water hexamer with (a) the edge-shared triangle configuration and (b,c) the edge-shared rhombic configurations adsorbed on Cu(111). The values represent their relative energies in kcal/mol with respect to the boat configuration.

4 Calculated apparent height difference

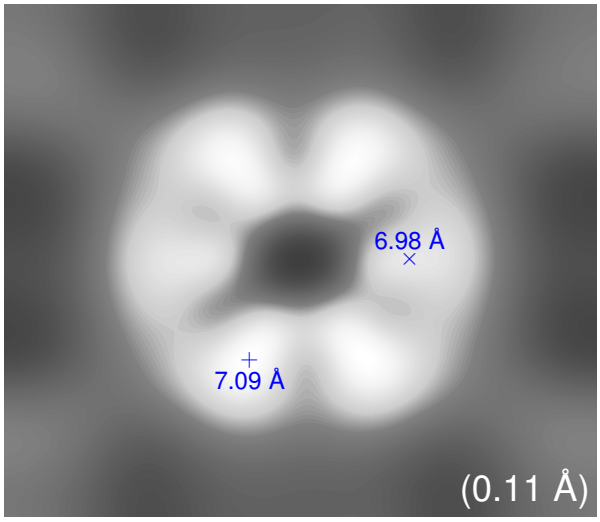

Figure S3: Calculated apparent height difference (the value in parentheses) among the petal-like patterns from the boat configuration with a high workfunction tip. The maximum is labeled as "+" and the minimum is labeled as "×".

5 Other site projected wave functions

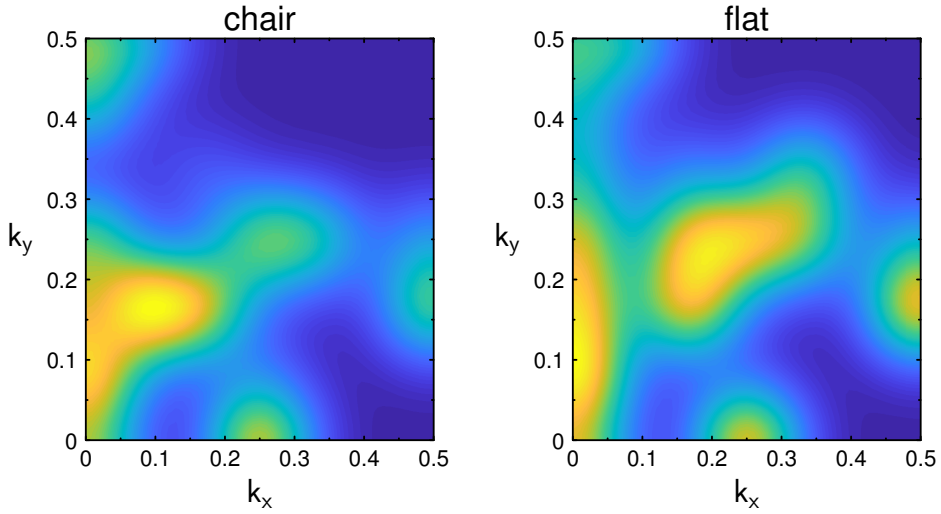

Figure S4: Site projected wave function on water hexamer within the bias window in the irreducible Brillouin zone for the chair (left) and the flat (right) configurations.

6 Molecular dynamics simulations under 13 K

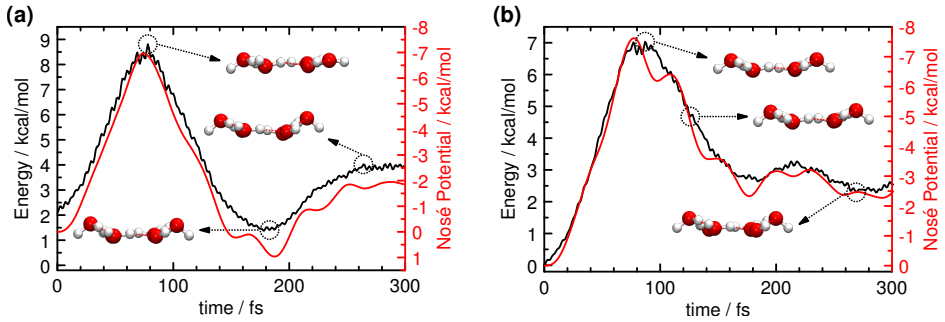

Figure S5: Calculated potential energies (black line) and the applied Nosé potentials along the time after contacting the Nosé thermostat for the flat (a) and boat (b) configurations, respectively. The temperature of the thermostat is set to 13 K. The representative geometries at different times after contacting the thermostat are depicted as the insets in (a) and (b). The Cu(111) surface is omitted in all present geometries for clarity.

7 Bader charge analysis

Table S1: Bader change analysis of water hexamer on Cu(111) surface with different configurations (Conf.). The negligible charge transfer between water hexamer and the inert substrate shown here allows the energy calibration as shown in Eq. S2.

Conf.	chair	boat	flat
W_1	0.0103	−0.0158	−0.0049
W_2	−0.0075	−0.0064	−0.0141
W_3	0.0113	0.0099	−0.0041
W_4	−0.0077	−0.0159	−0.0039
W_5	0.0094	−0.0060	−0.0150
W_6	−0.0185	0.0104	0.0005
Sum	−0.0027	−0.0238	−0.0415

8 Calculated adsorption energies with other functionals

Table S2: Calculated adsorption energies (in kcal/mol) of different water hexamer configurations at different theoretical levels. The most stable configurations are labeled in bold. The values in parentheses are the relative adsorption energies with respect to those of the chair configuration.

Theoretical Level	chair	boat	flat
vdW-DF2[a,b]	—	— (-1.88)	— (-3.83)
SCAN[a,b]	—	— **(0.04)**	— (-1.70)
XYG3[c,d]	76.82	**77.01 (0.19)**	76.85 (0.03)
ωB97X-2[c,e]	78.82	**78.98 (0.16)**	78.60 (-0.22)

[a] adsorption energy (Eq. S1)
[b] with plane wave basis sets
[c] water cluster calibrated adsorption energy (Eq. S2)
[d] with NAO-VCC-5Z
[e] extrapolated from aug-cc-pVTZ and QZ

9 Calculated frequencies

Table S3: Calculated frequencies in cm^{-1} of water hexamer on Cu(111) surface with different configurations.

No.	chair	boat	flat	No.	chair	boat	flat
1	50.33	56.89	71.24i	28	570.33	525.42	597.43
2	53.31	58.87	38.58i	29	578.70	600.33	607.18
3	55.34	59.45	63.77	30	579.81	630.00	649.93
4	84.89	79.39	64.46	31	780.72	763.64	690.48
5	85.53	97.31	67.85	32	782.03	779.44	703.87
6	98.65	99.23	86.46	33	812.97	816.80	746.36
7	103.00	102.01	90.27	34	978.65	822.61	749.31
8	104.40	124.69	91.58	35	981.20	980.22	772.48
9	126.17	127.47	97.08	36	1010.11	994.84	792.38
10	145.04	129.33	101.01	37	1582.82	1581.53	1588.89
11	147.55	143.79	116.34	38	1591.50	1587.33	1590.11
12	153.67	144.68	140.08	39	1591.83	1596.63	1593.22
13	181.47	164.68	161.84	40	1619.84	1605.32	1594.54
14	205.33	194.69	210.57	41	1620.12	1623.37	1601.91
15	206.92	239.98	221.65	42	1635.14	1626.11	1606.08
16	316.69	275.92	243.25	43	2754.14	2743.00	3087.87
17	317.61	338.17	257.99	44	2796.87	2759.42	3122.55
18	331.27	342.61	302.74	45	2802.58	3113.86	3179.62
19	346.09	355.73	312.71	46	3293.10	3115.29	3208.03
20	346.85	369.16	334.10	47	3297.37	3339.76	3258.04
21	373.11	392.24	335.75	48	3299.64	3340.36	3269.22
22	416.82	395.39	350.19	49	3579.84	3561.92	3671.89
23	440.55	412.44	358.51	50	3580.45	3562.51	3672.67
24	440.75	421.41	379.17	51	3581.99	3671.74	3673.85
25	461.34	442.32	397.76	52	3668.88	3671.85	3674.59
26	493.33	482.84	481.43	53	3670.34	3673.17	3675.14
27	494.51	516.54	484.24	54	3670.62	3673.51	3676.53

References

(S1) Klimeš, J.; Bowler, D. R.; Michaelides, A. Van der Waals Density Functionals Applied to Solids. *Phys. Rev. B* **2011**, *83*, 195131.

(S2) Kresse, G.; Furthmüller, J. Efficient Iterative Schemes for *ab initio* Total-Energy Calculations Using a Plane-Wave Basis Set. *Phys. Rev. B* **1996**, *54*, 11169–11186.

(S3) Lee, K.; Murray, É. D.; Kong, L.; Lundqvist, B. I.; Langreth, D. C. Higher-Accuracy van der Waals Density Functional. *Phys. Rev. B* **2010**, *82*, 081101.

(S4) Sun, J.; Remsing, R. C.; Zhang, Y.; Sun, Z.; Ruzsinszky, A.; Peng, H.; Zenghui, Y.; Paul, A.; Waghmare, U.; Wu, X.; Klein, M. L.; Perdew, J. P. Accurate First-Principles Structures and Energies of Diversely Bonded Systems From an Efficient Density Functional. *Nat. Chem.* **2016**, *8*, 831–836.

(S5) Lide, D. *CRC Handbook of Chemistry and Physics: A Ready-Reference Book of Chemical and Physical Data*; CRC Taylor & Francis: Boca Raton, Fla, 2006.

(S6) Liriano, M. L.; Gattinoni, C.; Lewis, E. A.; Murphy, C. J.; Sykes, E. C. H.; Michaelides, A. Water–Ice Analogues of Polycyclic Aromatic Hydrocarbons: Water Nanoclusters on Cu(111). *J. Am. Chem. Soc.* **2017**, *139*, 6403–6410.

(S7) Blöchl, P. E.; Jepsen, O.; Andersen, O. K. Improved Tetrahedron Method for Brillouin-Zone Integrations. *Phys. Rev. B* **1994**, *49*, 16223.

(S8) Kresse, G.; Joubert, D. From Ultrasoft Pseudopotentials to the Projector Augmented-Wave Method. *Phys. Rev. B* **1999**, *59*, 1758–1775.

(S9) Neugebauer, J.; Scheffler, M. Adsorbate-Substrate and Adsorbate-Adsorbate Interactions of Na and K Adlayers on Al(111). *Phys. Rev. B* **1992**, *46*, 16067–16080.

(S10) Makov, G.; Payne, M. C. Periodic Boundary Conditions in *ab initio* Calculations. *Phys. Rev. B* **1995**, *51*, 4014–4022.

(S11) Monkhorst, H. J.; Pack, J. D. Special Points for Brillouin-Zone Integrations. *Phys. Rev. B* **1976**, *13*, 5188–5192.

(S12) Methfessel, M.; Paxton, A. T. High-Precision Sampling for Brillouin-Zone Integration in Metals. *Phys. Rev. B* **1989**, *40*, 3616–3621.

(S13) Grimme, S. Supramolecular Binding Thermodynamics by Dispersion-Corrected Density Functional Theory. *Chem. Eur. J.* **2012**, *18*, 9955–9964.

(S14) Seitsonen, A. P.; Bryk, T. Melting Temperature of Water: DFT-Based Molecular Dynamics Simulations With D3 Dispersion Correction. *Phys. Rev. B* **2016**, *94*, 184111.

(S15) Frisch, M. J.; Trucks, G. W.; Schlegel, H. B.; Scuseria, G. E.; Robb, M. A.; Cheeseman, J. R.; Scalmani, G.; Barone, V.; Mennucci, B.; Petersson, G. A.; Nakatsuji, H.; Caricato, M.; Li, X.; Hratchian, H. P.; Izmaylov, A. F.; Bloino, J.; Zheng, G.; Sonnenberg, J. L.; Hada, M.; Ehara, M.; Toyota, K.; Fukuda, R.; Hasegawa, J.; Ishida, M.; Nakajima, T.; Honda, Y.; Kitao, O.; Nakai, H.; Vreven, T.; Montgomery, J. A., Jr.; Peralta, J. E.; Ogliaro, F.; Bearpark, M.; Heyd, J. J.; Brothers, E.; Kudin, K. N.; Staroverov, V. N.; Kobayashi, R.; Normand, J.; Raghavachari, K.; Rendell, A.; Burant, J. C.; Iyengar, S. S.; Tomasi, J.; Cossi, M.; Rega, N.; Millam, J. M.; Klene, M.; Knox, J. E.; Cross, J. B.; Bakken, V.; Adamo, C.; Jaramillo, J.; Gomperts, R.; Stratmann, R. E.; Yazyev, O.; Austin, A. J.; Cammi, R.; Pomelli, C.; Ochterski, J. W.; Martin, R. L.; Morokuma, K.; Zakrzewski, V. G.; Voth, G. A.; Salvador, P.; Dannenberg, J. J.; Dapprich, S.; Daniels, A. D.; Farkas, Ö.; Foresman, J. B.; Ortiz, J. V.; Cioslowski, J.; Fox, D. J. Gaussian 09 Revision A. 02. 2009; Gaussian Inc. Wallingford CT.

(S16) Chai, J.-D.; Head-Gordon, M. Long-Range Corrected Double-Hybrid Density Functionals. *J. Chem. Phys.* **2009**, *131*, 174105.

(S17) Blum, V.; Gehrke, R.; Hanke, F.; Havu, P.; Havu, V.; Ren, X.; Reuter, K.; Scheffler, M.

Ab initio Molecular Simulations With Numeric Atom-Centered Orbitals. *Comput. Phys. Commun.* **2009**, *180*, 2175–2196.

(S18) Shen, T.; Zhu, Z.; Zhang, I. Y.; Scheffler, M. Massive-Parallel Implementation of the Resolution-of-Identity Coupled-Cluster Approaches in the Numeric Atom-Centered Orbital Framework for Molecular Systems. *J. Chem. Theory Comput. 15*, 4721–4734.

(S19) Zhang, I. Y.; Ren, X.; Rinke, P.; Blum, V.; Scheffler, M. Numeric atom-centered-orbital basis sets with valence-correlation consistency from H to Ar. *New J. Phys. 15*, 123033.

(S20) Tersoff, J.; Hamann, D. R. Theory of the Scanning Tunneling Microscope. *Phys. Rev. B* **1985**, *31*, 805–813.

(S21) Hofer, W. A.; Foster, A. S.; Shluger, A. L. Theories of Scanning Probe Microscopes at the Atomic Scale. *Rev. Mod. Phys.* **2003**, *75*, 1287–1331.

(S22) Carrasco, J.; Michaelides, A.; Forster, M.; Haq, S.; Raval, R.; Hodgson, A. A One-Dimensional Ice Structure Built From Pentagons. *Nat. Mater.* **2009**, *8*, 427–431.

(S23) Bader, R. *Atoms in Molecules: A Quantum Theory*; Clarendon Press: Oxford New York, 1990.

(S24) Tang, W.; Sanville, E.; Henkelman, G. A Grid-Based Bader Analysis Algorithm without Lattice Bias. *J. Phys.: Condens. Matter* **2009**, *21*, 084204.

(S25) Morgenstern, K.; Rieder, K.-H. Formation of The Cyclic Ice Hexamer Via Excitation of Vibrational Molecular Modes by The Scanning Tunneling Microscope. *J. Chem. Phys.* **2002**, *116*, 5746–5752.

(S26) Michaelides, A.; Morgenstern, K. Ice Nanoclusters at Hydrophobic Metal Surfaces. *Nat. Mater.* **2007**, *6*, 597–601.

(S27) Guo, Y.; Ding, Z.; Sun, L.; Li, J.; Meng, S.; Lu, X. Inducing Transient Charge State of a Single Water Cluster on Cu(111) Surface. *ACS Nano* **2016**, *10*, 4489–4495.